Research Square

Preprints are preliminary reports that have not undergone peer review.
They should not be considered conclusive, used to inform clinical practice,
or referenced by the media as validated information.

Dynamic reliability assessment of aero-engine components using dependence-aware PNET and mechanism-informed aging correction

Yongzhen Yang

860586614@qq.com

Jinan University

Ruiguan Lin

AVIC China Aero-Polytechnology Establishment

Jiayi Zhang

Jinan University

Ruwei Luo

Tsinghua University

Xian Wu

China Southern Technic

Yusen Lin

China Southern Technic

Article

Keywords: Aero-engine, probabilistic network evaluation technique, equivalent damage time, correlated failure modes, dynamic reliability assessment, aging correction

Posted Date: August 27th, 2026

DOI: https://doi.org/10.21203/rs.3.rs-10584266/v1

License: This work is licensed under a Creative Commons Attribution 4.0 International License.
Read Full License

Additional Declarations: No competing interests reported.

Dynamic reliability assessment of aero-engine components using dependence-aware PNET and mechanism-informed aging correction

Yongzhen Yang[1], Ruiguan Lin[2,3], Jiayi Zhang[1], Ruwei Luo[4], Xian Wu[5], Yusen Lin[5]

1. School of Cyberspace Security, Jinan University, Guangzhou 511443, China

2. AVIC China Aero-Polytechnology Establishment, Beijing 100028, China

3. Key Laboratory of Quality Infrastructure Efficacy Research, State Administration for Market Regulation, Beijing 100028, China

4. Department of Industrial Engineering, Tsinghua University, Beijing 100084, China

5. China Southern Technic, Guangzhou 510403, China

Corresponding author: Yongzhen Yang. E-mail: 860586614@qq.com

Abstract

Aero-engine hot-section components are subjected to complex thermal, mechanical, vibrational, contact and environmental loads. Multiple degradation mechanisms may coexist, interact and evolve during service, making conventional independent multi-mode reliability models potentially inaccurate. Independent product models may repeatedly count common-cause risks among physically related failure modes, whereas models based only on calendar time or operating hours may underestimate damage acceleration under severe mission profiles. This study proposes a dynamic reliability assessment framework for aero-engine components by integrating dependence-aware PNET with mechanism-informed equivalent damage-time correction. A composite dependence-similarity score is constructed from three terms: common-load-induced dependence, failure-rate proximity and lifetime-distribution overlap. At each service-time node, failure modes are represented as a thresholded graph, clustered according to dependence similarity and reduced to representative modes. Equivalent damage-time correction is then introduced to transform operating time into a mechanism-informed damage scale. A sanitized high-pressure turbine blade-disk assembly is used as the case study. Four reliability models are compared to distinguish the separate and combined effects of dependence screening and aging correction: full-mode independent reliability without aging correction, representative-mode reliability without aging correction, full-mode independent reliability with aging correction and representative-mode reliability with aging correction. The results show that dependence-aware representative-mode screening mitigates repeated counting of positively dependent failure paths, whereas equivalent damage-time correction accounts for accelerated degradation under actual operating profiles. The proposed framework provides an interpretable and extensible approach for reliability assessment of dependent degradation processes in aero-engine components.

Key words

Aero-engine; probabilistic network evaluation technique; equivalent damage time; correlated failure modes; dynamic reliability assessment; aging correction.

Introduction

Aero-engines are safety-critical systems composed of multiple interacting subsystems, including compressors, combustors, turbines, shafts, bearings, accessories and control systems. Among these, hot-section components such as turbine blades, turbine disks and blade-disk attachment structures are particularly important because they operate under high temperature, high rotational speed, strong thermal gradients, aerodynamic excitation and complex mechanical loading. Nickel-based superalloy hot-section components are susceptible to low-cycle fatigue, high-cycle fatigue, thermomechanical fatigue, creep and oxidation under combined thermal and mechanical loading[1-4]. Thermal-barrier coatings may additionally fail through thermally grown oxide formation, interfacial cracking and spallation[5], whereas attachment regions and impacted airfoils are susceptible to fretting fatigue and foreign-object-damage-assisted fatigue[6-12].

The degradation of aero-engine hot-section components is rarely governed by a single isolated mechanism. Different local regions may experience coupled thermal, mechanical, vibrational, contact and environmental loading. These combined loading conditions may lead to interacting degradation processes such as creep-fatigue-oxidation interaction, high-cycle fatigue, fretting fatigue, contact fatigue and coating degradation[6-11]. Different failure modes may therefore share common driving variables even when their dominant physical mechanisms differ. Such common-cause variables can induce statistical dependence among failure modes and make independent multi-mode reliability approximations questionable.

Conventional component reliability models often represent multi-mode failure using independent series-system approximations, fault trees or separate marginal lifetime distributions. Classical structural system reliability methods address multiple potentially correlated failure modes through reliability bounds, representative events and reduced-order approximations[13-17]. However, aero-engine components operate under variable mis-

sion profiles, and shared operating environments, common random factors and environmental covariates may induce dependence among multiple degradation processes[18,19]. The dependence structure may also evolve with load history, environmental exposure and accumulated damage[20,21]. Consequently, treating correlated modes as independent may repeatedly count common-cause risk, whereas imposing a fixed dependence structure may fail to capture changes in dominant degradation mechanisms over service life.

PNET-type representative-event concepts were introduced in early structural system reliability studies by Ma and Ang[16] and were subsequently discussed in engineering reliability texts[17]. Their core idea is to group highly dependent or highly similar failure events and represent each group using a dominant event. PNET-type screening can reduce the computational burden of system reliability evaluation when direct calculation of high-dimensional joint failure probabilities is difficult. Nevertheless, conventional PNET applications often rely on a single correlation coefficient and a fixed threshold. For complex engineering components, dependence may arise not only from statistical correlation but also from similarity in instantaneous risk levels and lifetime evolution patterns. Therefore, a more interpretable dependence-screening metric is needed.

Another limitation of many reliability models is the direct use of calendar time, operating hours or cycles as the time variable. In physics-of-failure analysis, damage accumulation depends not only on elapsed time but also on stress or strain amplitude, temperature, dwell time, vibration state, contact pressure, material state and environmental exposure. Fatigue damage is related to cyclic stress or strain history, creep damage is strongly temperature and dwell-time-dependent, and contact-interface damage depends on local contact and slip conditions. As a result, directly substituting operating time into a baseline lifetime distribution may not represent the effective aging rate of a component under a specific mission profile.

Cumulative-damage and accelerated-life concepts provide a practical basis for transforming actual load histories into an equivalent damage-time scale[22-27]. For creep-dominated failure, time-temperature equivalence has a specific physical basis in classical rupture-parameter formulations[28]. For aircraft engines, operational severity and component life consumption are strongly affected by thermal, rotational and mission-profile variables[29,30]. However, such aging correction is rarely integrated with dynamic dependence screening among multiple failure modes. Performance-based health monitoring, machinery prognostics and remaining-useful-life estimation provide the broader condition-based-maintenance context for dynamic reliability assessment[31-33].

This study proposes a dynamic reliability assessment framework for aero-engine components by combining dependence-aware PNET with mechanism-informed equivalent damage-time correction. A composite dependence-similarity score is constructed from common-load-induced statistical dependence, failure-rate proximity and lifetime-distribution overlap. At discrete service-time nodes, failure modes are represented as a thresholded graph, clustered according to dependence similarity and reduced to representative modes using weighted failure-rate and graph-centrality measures. For representative modes, calendar time is transformed into equivalent damage time through mechanism-specific aging coefficients.

The main contributions of this study are as follows. First, a composite dependence-similarity score is proposed for screening correlated aero-engine failure modes. The score integrates common-load-induced dependence, failure-rate proximity and lifetime-distribution overlap. Second, a dynamic PNET procedure is developed to identify time-varying representative failure modes at discrete service-time nodes. Third, mechanism-informed equivalent damage-time correction is incorporated into representative-mode reliability calculation to account for average degradation acceleration under actual operating profiles. Fourth, a unified four-model comparison framework is established to distinguish the separate and combined effects of dependence screening and aging correction. Fifth, a sanitized aero-engine hot-section component case study is used to demonstrate the applicability of the proposed framework.

Methods

Overview of the proposed framework

The proposed framework consists of four modules: marginal lifetime modelling, dependence-similarity evaluation, dynamic representative-mode screening and aging-corrected reliability comparison.

First, candidate lifetime distributions are fitted for each failure mode using failure and right-censored observations. Second, a composite dependence-similarity score is calculated by combining common-load-induced dependence, failure-rate proximity and lifetime-distribution overlap. Third, at each service-time node, the dependence-similarity matrix is converted into a thresholded graph, and connected components are treated as dependence-similarity clusters. A representative failure mode is then selected from each cluster. Finally, four reliability models are compared to distinguish the effects of dependence screening and aging correction.

The overall workflow is shown in Figure 1.

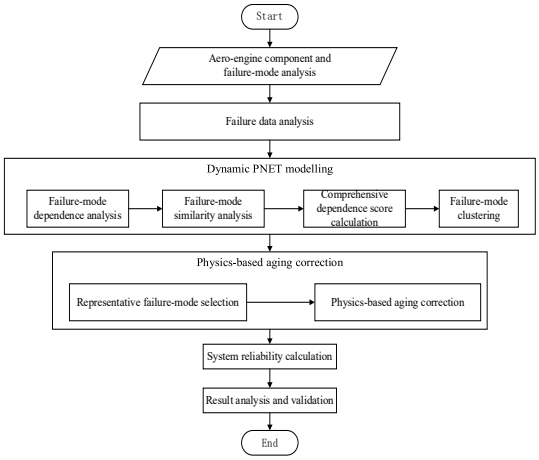


Figure 1. Overall workflow of the proposed dynamic reliability assessment framework.

System representation and failure-mode set

Let the candidate failure-mode set be

$$M=\{M_1, M_2, \cdots, M_n\} \tag{1}$$

Each failure mode M_i is associated with a lifetime random variable T_i, a marginal reliability function $R_i(t)$, a density function $f_i(t)$, and an instantaneous failure rate $\lambda_i(t)$.

For a full-mode independent series approximation, the system reliability is

$$R_{all}(t) = \prod_{i=1}^{n} R_i(t) \tag{2}$$

This approximation is useful as a baseline model. However, when multiple failure modes are driven by shared loads or physically similar degradation processes, direct multiplication may repeatedly count common-cause risk. Therefore, the proposed method uses dependence-aware representative-mode screening before system reliability evaluation.

If the underlying system logic is more complex than a series approximation, the proposed PNET procedure should be regarded as a dimension-reduction step before performing the corresponding system-logic or fault-tree calculation.

Common-cause load-induced dependence

Assume that the logarithmic lifetime of each failure mode is influenced by a vector of common load-environment variables X. A local logarithmic lifetime model can be written as $lnT_i = b_i + a_i^T(t)X + \varepsilon_i$, where b_i is an intercept, $a_i(t)$ is the time-dependent sensitivity vector, and ε_i is a mode-specific random error.

If Σ_X denotes the covariance matrix of X, the common-cause load-induced dependence between modes M_i and M_j is approximated by

$$\rho_{ij}^{load}(t) = \frac{a_i^T(t)\Sigma_X a_j(t)}{\sqrt{a_i^T(t)\Sigma_X a_i(t)}\sqrt{a_j^T(t)\Sigma_X a_j(t)}} \tag{3}$$

Only positive dependence is used for representative-mode screening $\rho_{ij}^{load,+}(t) = max\{\rho_{ij}^{load}(t), 0\}$.

This truncation is appropriate when the aim is to avoid repeated counting of positively dependent or physically similar failure paths. If strong negative dependence exists, a full joint reliability model should be considered.

Failure-rate proximity

Failure-rate proximity measures whether two modes have similar instantaneous risk levels at time t:

$$s_{ij}^{\lambda}(t) = 1 - \frac{|\lambda_i(t) - \lambda_j(t)|}{max\{\lambda_i(t), \lambda_j(t)\} + \varepsilon} \tag{4}$$

Here, ε is a small positive constant used to avoid division by zero. The value of $s_{ij}^{\lambda}(t)$ approaches 1 when two modes have similar failure rates and approaches 0 when their instantaneous risk levels differ substantially.

Lifetime-distribution overlap

The lifetime-distribution overlap between two modes is defined as

$$s_{ij}^{dist} = \int_0^{+\infty} min\{f_i(u), f_j(u)\}\, du \tag{5}$$

This coefficient ranges from 0 to 1 and measures the similarity between two marginal lifetime densities. It is not a direct stochastic dependence measure. When parametric lifetime distributions are available, the integral

can be evaluated by numerical quadrature. If no explicit parametric distribution is available, density estimation may be performed on a transformed time scale.

Composite dependence-similarity score

The composite dependence-similarity score is defined as:

$$d_{ij}(t) = \omega_{load}\rho_{ij}^{load,+}(t) + (1-\omega_{load})[\omega_{\lambda}s_{ij}^{\lambda}(t) + \omega_{dist}s_{ij}^{dist}] \quad (6)$$

The weights satisfy $\omega_{\lambda} + \omega_{\mathrm{dist}} = 1$ and $0 \le \omega_{\mathrm{load}} \le 1$. The score $d_{ij}(t)$ is symmetric and bounded between 0 and 1 if all component scores are bounded between 0 and 1. It is used as an engineering screening metric and should not be interpreted as a Pearson correlation coefficient, a rank correlation coefficient or a copula parameter.

Dynamic PNET clustering and representative-mode selection

At each service-time node t_k, the dependence-similarity matrix $D(t_k) = [d_{ij}(t_k)]_{n\times n}$ is constructed. For a threshold r, an undirected graph $G(t_k; r)$ is built by connecting two modes if $d_{ij}(t_k) \ge r$. The connected components of this graph are treated as dependence-similarity clusters.

The graph-based representative-mode selection procedure is shown in Figure 2.

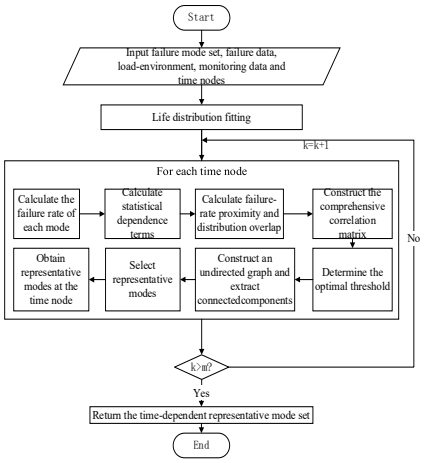


Figure 2. Graph-based representative-mode selection procedure.

The threshold r may be selected using prior engineering knowledge, validation against historical reliability data or sensitivity analysis. A larger threshold produces more clusters and fewer merged modes, whereas a smaller threshold produces larger clusters and stronger representative-mode reduction.

For a cluster $C_l(t_k)$, the representative mode is selected by

$$M_l^{rep}(t_k) = arg\max_{M_p \in C_l(t_k)}[\alpha\frac{\lambda_p(t_k)}{max_q\,\lambda_q(t_k)} + (1-\alpha)\frac{1}{|C_l(t_k)|-1}\sum_{q\in C_l(t_k),q\neq p} d_{pq}(t_k)] \quad (7)$$

Here, $0 \le \alpha \le 1$. The first term represents normalized instantaneous risk, and the second term represents graph centrality within the cluster. If a cluster contains only one mode, that mode is directly selected as its representative.

The representative-mode set at t_k is denoted as

$$M_{rep}(t_k) = \{M_1^{rep}(t_k), M_2^{rep}(t_k), \cdots, M_{L_k}^{rep}(t_k)\}$$

where L_k is the number of clusters.

Equivalent damage-time correction

Equivalent damage-time correction transforms calendar or operating time into a mechanism-informed damage scale. The schematic concept is shown in Figure 3.

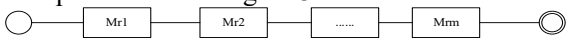


Figure 3. Schematic illustration of equivalent damage-time correction.

For failure mode M_i, the equivalent damage time is defined as

$$\tau_i(t) = \int_0^t A_i(S(u), \Theta_i)du \approx \kappa_i t \quad (8)$$

where $A_i(S(u), \Theta_{\mathrm{i}})$ is a dimensionless acceleration factor, $S(u)$ is the load-environment state vector and Θ_i represents mechanism-specific parameters, and κ_i is an average aging coefficient.

The aging-corrected reliability is then written as

$$R_i^*(t) = R_i(\tau_i(t)) \approx R_i(\kappa_i t)$$

If $\kappa_i > 1$, degradation proceeds faster than the baseline time scale; if $\kappa_i < 1$, degradation proceeds more slowly.

The aging coefficient can be estimated using failure and right-censored observations. In Bayesian implementation, a weakly informative prior may be assigned to $ln\kappa_i$, and the posterior mean of κ_i can be used as the point estimate. Because κ_i may be confounded with the scale parameter of the lifetime distribution, independent baseline information, informative priors or hierarchical constraints are recommended.

The equivalent damage-time correction used here is an engineering approximation. It does not replace detailed physics-of-failure modelling, but it provides a practical way to account for average degradation acceleration when full load spectra or high-fidelity damage simulations are not available.

Comparative reliability models

To distinguish the effects of dependence screening and aging correction, four reliability models are defined.

$$\begin{gathered} Model\ A\colon R_A(t) = \prod_{M_i \in M} R_i(t) \\ Model\ B\colon R_B(t) = \prod_{M_i \in M_{rep}(t)} R_i(t) \\ Model\ C\colon R_C(t) = \prod_{M_i \in M} R_i^*(t) \\ Model\ D\colon R_D(t) = \prod_{M_i \in M_{rep}(t)} R_i^*(t) \end{gathered} \tag{10}$$

Model A is the full-mode independent product without aging correction. Model B applies dynamic representative-mode screening but does not apply aging correction. Model C applies aging correction to all failure modes but does not apply representative-mode screening. Model D combines dynamic representative-mode screening and aging correction.

When the representative-mode set changes with service time, direct switching may cause artificial discontinuities in reliability. Therefore, switching can be smoothed at the cumulative-hazard level. If a cluster representative changes from M_a to M_b near switching time t_s, the smoothed cumulative hazard contribution is

$$H_{sw}(t) = [1 - \omega(t)]H_a^*(t) + \omega(t)H_b^*(t), \omega(t) = \frac{1}{1+exp[-\gamma(t-t_s)]} \tag{11}$$

Here, γ controls the transition width. This cumulative-risk-based smoothing avoids non-physical reliability jumps and prevents repeated accumulation of switching-mode risk. For models without aging correction, $H_a^*(t)$ and $H_b^*(t)$ in Equation (11) are replaced by their uncorrected cumulative hazards.

Model diagnostics and robustness analysis

Cox-Snell residual diagnostics are used to examine the adequacy of fitted lifetime and aging-corrected survival models. For observation j of mode M_i, the Cox-Snell residual is

$$e_{ij} = -ln\widehat{R_{i,0}}(\hat{\kappa}_i t_{ij}) \tag{12}$$

Under a correctly specified model, the residuals should approximately follow a unit exponential distribution. With censored data, the cumulative hazard of residuals can be estimated using the Nelson-Aalen estimator and compared with the 45-degree reference line.

Variance-based sensitivity analysis is used to quantify the influence of uncertain aging coefficients on system reliability. If the model output is $Y = R_{sys}(t_0)$, the total-order Sobol index of input θ_i is

$$S_{T_i} = 1 - \frac{Var_{\theta_i}[E(Y|\theta_i)]}{Var(Y)} \tag{13}$$

A copula-based Monte Carlo benchmark can additionally be used to examine the possible effect of dependence among failure modes. For generated sample m, let $T_i^{(m)}$ denote the sampled lifetime of mode M_i. The joint survival probability is estimated as

$$\hat{R}_{MC}(t) = \frac{1}{N}\sum_{m=1}^{N} I(T_1^{(m)} > t, \cdots, T_n^{(m)} > t) \tag{14}$$

The copula benchmark should be interpreted as a robustness comparison unless the dependence parameters are directly estimated from suitable joint lifetime data.

Experiments

Case-study object and failure modes

A sanitized high-pressure turbine blade-disk assembly from an in-service turbofan engine fleet was used as the case study. The assembly consists of first-stage rotor blades made of a directionally solidified nickel-based superalloy and a turbine disk made of powder-metallurgy nickel-based superalloy. The blades and disk are connected through a fir-tree attachment structure.

The schematic structure of the case-study assembly is shown in Figure 4. Typical weak regions include the blade transition region, cooling-hole region, fir-tree tenon-slot contact interface, disk slot, blade tip and coating interface. The blades are subjected to centrifugal force, aerodynamic excitation, thermal shock and high-temperature oxidation or corrosion. The disk slot region experiences alternating contact loads transmitted

through the blade attachment. Therefore, the blade-disk assembly forms a contact-coupled failure system involving several interacting degradation mechanisms.

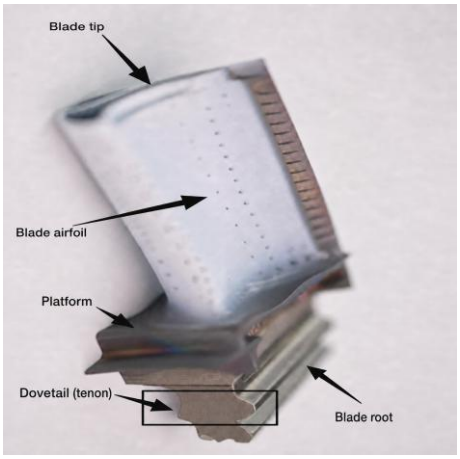


Figure 4. Schematic structure of the high-pressure turbine blade-disk assembly.

In this study, the term failure mode refers to an inspection-detectable degradation or damage event that can trigger maintenance action or contribute to the top event. It does not necessarily imply immediate engine-level failure. Based on failure mode and effects analysis, maintenance engineering records and established damage-mechanism literature[4,5,8-12,28], seven major failure modes were identified. These modes are listed in Table 1.

Table 1. Failure modes of the case-study blade-disk assembly.

Mode	Failure mode	Main affected region	Dominant mechanism
M_1	Blade low-cycle fatigue cracking	Blade root or transition region	Cyclic plasticity and thermal-mechanical fatigue
M_2	Blade high-cycle fatigue cracking	Airfoil or blade root	Vibration-induced fatigue
M_3	Tenon fretting wear	Fir-tree attachment interface	Contact wear and fretting fatigue
M_4	Disk slot crack	Disk fir-tree slot	Contact stress and fatigue cracking
M_5	Coating spallation	Blade coating interface	Oxidation, thermal mismatch and interfacial cracking
M_6	Foreign-object-damage-assisted cracking	Blade leading edge or airfoil	Impact damage and fatigue crack initiation
M_7	Creep rupture	High-temperature blade region	Time-dependent creep damage

The fault tree for blade fracture or liberation is shown in Figure 5. In the numerical demonstration, a representative-mode series approximation was used after PNET screening. When the underlying fault tree contains strong AND-gate structures or non-series logic, the fault-tree calculation should be performed after representative-mode screening rather than replaced by a series approximation.

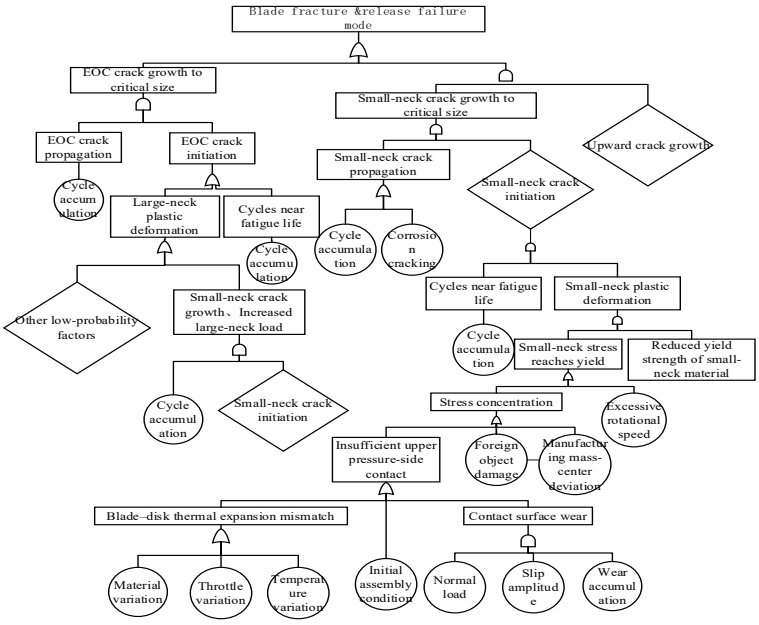


Figure 5. Fault tree for blade fracture or liberation of the high-pressure turbine blade-disk assembly.

Lifetime distribution fitting

Fleet failure records, borescope inspection records, right-censored samples, aggregated operating profiles and normalized load-environment variables were used for lifetime modelling. Engine serial numbers and commercially sensitive background information were removed. Time since new, measured in flight hours, was used as the main lifetime variable.

For each failure mode, Weibull, lognormal and exponential distributions were considered as candidate lifetime distributions. Right censoring was included in the likelihood function. The final distribution type was selected according to the maximized log-likelihood, Akaike information criterion, graphical diagnostics and consistency with the corresponding failure mechanism.

The fitted lifetime distributions are summarized in Table 2.

Table 2. Fitted marginal lifetime distributions of the seven failure modes.

Mode	Distribution type	Parameters	Mechanism consistency
M_1	Weibull	Shape parameter β=3.915, scale parameter η=8670.518	Increasing hazard due to fatigue accumulation
M_2	Weibull	Shape parameter β=6.657, scale parameter η=10356.964	Vibration fatigue with accumulated crack initiation risk
M_3	Weibull	Shape parameter β=2.466, scale parameter η=9476.042	Progressive wear and fretting damage
M_4	Lognormal	Log-mean μ=9.185, log-standard deviation σ=0.390	Crack initiation and growth in disk slot
M_5	Weibull	Shape parameter β=3.082, scale parameter η=11732.897	Multiplicative coating degradation process
M_6	Exponential	Failure rate λ=2.646×10-5	Random impact-assisted initiation with possible aging effect
M_7	Lognormal	Log-mean μ=9.105, log-standard deviation σ=0.584	Time-temperature-dependent creep damage

The fitted distributions were subsequently used to compute marginal reliability functions, probability density functions and instantaneous failure rates for dependence-similarity analysis.

Dependence-similarity matrix and representative modes at 5000 FH

For the case-study blade-disk assembly, the load-environment driving vector was specified as $X = [T_g, \Omega, A_v, p_c, C_e]^T$, where T_g is the equivalent turbine inlet temperature indicator, Ω is the equivalent rotational speed or centrifugal load indicator, A_v is the vibration amplitude indicator, p_c is the tenon-slot contact pressure indicator, and C_e is the corrosion or oxidation environment indicator. All variables are normalized using the fleet operational database.

Using Equations (3)-(6), the dependence-similarity matrix was calculated at each service-time node. The resulting matrix at 5000 FH is shown in Table 3.

Table 3. Composite dependence-similarity matrix at 5000 FH.

Mode	M_1	M_2	M_3	M_4	M_5	M_6	M_7
M_1	1.000	0.664	0.831	0.503	0.714	0.650	0.580
M_2	0.664	1.000	0.712	0.479	0.780	0.676	0.472
M_3	0.831	0.712	1.000	0.481	0.787	0.641	0.589
M_4	0.503	0.479	0.481	1.000	0.502	0.520	0.622
M_5	0.714	0.780	0.787	0.502	1.000	0.722	0.538
M_6	0.650	0.676	0.641	0.520	0.722	1.000	0.513
M_7	0.580	0.472	0.589	0.622	0.538	0.513	1.000

Based on the selected dependence-similarity threshold, the graph was decomposed into dependence-similarity clusters. The representative mode in each cluster was then selected using Equation (7). The clustering and representative-mode selection results at 5000 FH are summarized in Table 4.

Table 4. Dependence-similarity clusters and representative modes at 5000 FH.

Cluster	Included modes	Representative mode	Main reason for selection
Cluster 1	$M_1, M_2, M_3, M_4, M_5, M_6$	M_3	High instantaneous risk and strong centrality in the attachment-related degradation group
Cluster 2	M_7	M_7	Single-mode cluster associated with high-temperature time-dependent degradation

The representative-mode set at 5000 FH was therefore composed of two modes, representing the main contact-coupled degradation group and the high-temperature creep-related degradation path.

Dynamic evolution of representative modes

The service interval from 500 to 15000 FH was divided into time nodes. The initial point $t = 0$ was used only as the reliability boundary condition $R(0) = 1$, not as a node for failure-rate-based centrality calculation, because several lifetime models have zero or singular hazards near the origin.

At each node, the load-environment covariance matrix, sensitivity vectors, failure rates, failure-rate proximity values and dependence-similarity matrix were updated according to the procedure described in Methods. The evolution of selected dependence-similarity scores is shown in Figure 6.

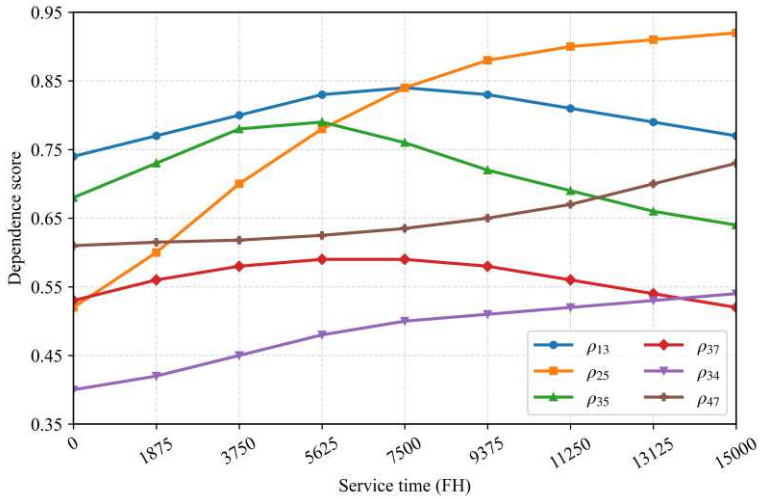


Figure 6. Evolution of selected dependence-similarity scores with service time.

The dynamic representative-mode results are summarized in Table 5.

Table 5. Dynamic evolution of representative modes.

Service-time interval	Main representative mode	Secondary representative mode	Interpretation
Early service	M_3	M_7	Contact-interface degradation and creep-related degradation dominate different clusters
Middle service	M_3	M_7	Representative structure remains stable
Late service	M_3	M_4	Disk slot cracking becomes more influential in the secondary degradation group

The secondary representative mode changed from M_7 to M_4 during late service. To avoid artificial reliability discontinuity, the switching center was taken as the midpoint between the two adjacent service nodes:

$$t_s = \frac{11250 + 13125}{2} = 12187.5\ FH$$

The logistic smoothing strategy in Equation (11) was then applied during reliability calculation.

Aging correction coefficients

The aging correction coefficients were estimated for each failure mode using the equivalent damage-time correction method described in Section Equivalent damage-time correction. The posterior distributions of the key representative-mode aging coefficients are shown in Figure 7.

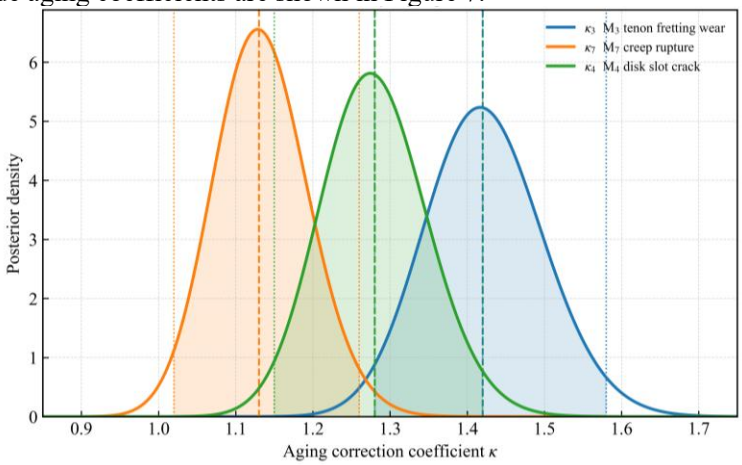


Figure 7. Posterior distributions of the key aging correction coefficients.

The posterior means of all aging coefficients are summarized in Table 6.

Table 6. Estimated aging correction coefficients of the seven failure modes.

Mode	Aging coefficient $\hat{\kappa}_i$	Failure mechanism
M_1	1.08	Fatigue aging correction under the observed mission profile
M_2	1.16	Vibration-related aging correction
M_3	1.42	Fretting-related aging correction
M_4	1.28	Disk-slot cracking aging correction
M_5	1.10	Coating degradation aging correction
M_6	1.19	Impact-assisted cracking aging correction
M_7	1.13	Creep-related aging correction

The posterior summaries of the main representative-mode aging coefficients are shown in Table 7.

Table 7. Posterior summaries of representative-mode aging coefficients.

Mode	Posterior mean	Standard deviation	95% credible interval	Engineering implication
M_3	1.42	0.077	[1.28, 1.58]	Dominant uncertainty source for contact-interface degradation
M_7	1.13	0.061	[1.02, 1.26]	High-temperature time-dependent degradation
M_4	1.28	0.069	[1.15, 1.42]	Late-service disk-slot cracking risk

The aging coefficients indicate whether the observed service profile accelerates or decelerates degradation relative to the baseline lifetime scale. Coefficients greater than one imply accelerated damage accumulation, whereas coefficients less than one imply slower damage accumulation.

Reliability comparison of the four models

The four reliability models defined in Section 2.9 were instantiated for the case-study blade-disk assembly.

For Model A, all seven case-study failure modes were included and directly combined under the independent product approximation. For Model B, the dynamic PNET procedure was applied first, and only the representative modes selected at each service-time node were used in the reliability calculation. For Model C, aging correction was applied to all seven failure modes, but no representative-mode reduction was performed. For Model D, dynamic PNET screening and aging correction were both applied.

The representative-mode set changed during late service. Therefore, the cumulative-hazard smoothing strategy in Equation (11) was used to avoid artificial reliability discontinuities during the transition between representative modes.

The reliability curves of the four models are shown in Figure 8, and the corresponding numerical values are listed in Table 8.

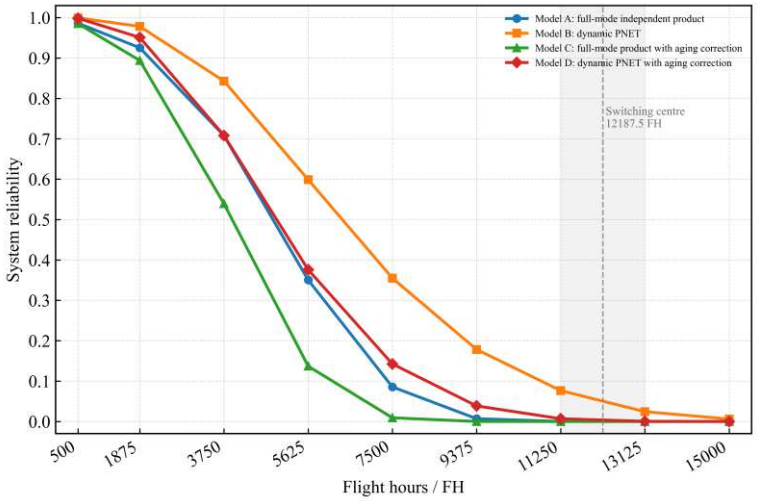


Figure 8. Reliability curves of Models A-D over the service interval.

Table 8. Reliability comparison of the four models.

FH	Model A	Model B	Model C	Model D
500	9.861×10^{-1}	9.993×10^{-1}	9.851×10^{-1}	9.983×10^{-1}
1875	9.253×10^{-1}	9.782×10^{-1}	8.939×10^{-1}	9.509×10^{-1}
3750	7.077×10^{-1}	8.429×10^{-1}	5.392×10^{-1}	7.081×10^{-1}
5625	3.504×10^{-1}	5.989×10^{-1}	1.370×10^{-1}	3.758×10^{-1}
7500	8.563×10^{-2}	3.550×10^{-1}	9.218×10^{-3}	1.425×10^{-1}
9375	6.996×10^{-3}	1.784×10^{-1}	7.826×10^{-5}	3.859×10^{-2}
11250	9.268×10^{-5}	7.645×10^{-2}	2.004×10^{-8}	6.857×10^{-3}
13125	5.303×10^{-8}	2.439×10^{-2}	1.179×10^{-14}	4.563×10^{-4}
15000	1.375×10^{-13}	6.052×10^{-3}	2.089×10^{-25}	2.065×10^{-5}

The results show that Model B gives higher reliability than Model A because representative-mode screening reduces repeated counting of positively dependent or physically similar failure paths. In contrast, Model C gives lower reliability than Model A because aging correction evaluates the modes on an accelerated damage-time scale. Model D combines these two effects and therefore provides the complete proposed estimate.

The difference between Model A and Model B reflects the effect of dependence-aware representative-mode screening. The difference between Model A and Model C reflects the effect of equivalent damage-time correction. The difference between Model B and Model D reflects the aging correction effect after dependence-aware dimension reduction.

Diagnostics, benchmark and robustness checks

Additional diagnostic, benchmark and robustness analyses were performed using desensitized and aggregated data. This section reports the corresponding results and engineering interpretations. Methodological definitions and calculation procedures have already been described in the Methods section and are therefore not repeated here.

Cox–Snell residual diagnostics

Cox–Snell residual diagnostics were performed for the main representative modes M_3, M_7 and M_4. The residual diagnostic curves are shown in Figure 9, and the corresponding residual-sample summary is listed in Table 9.

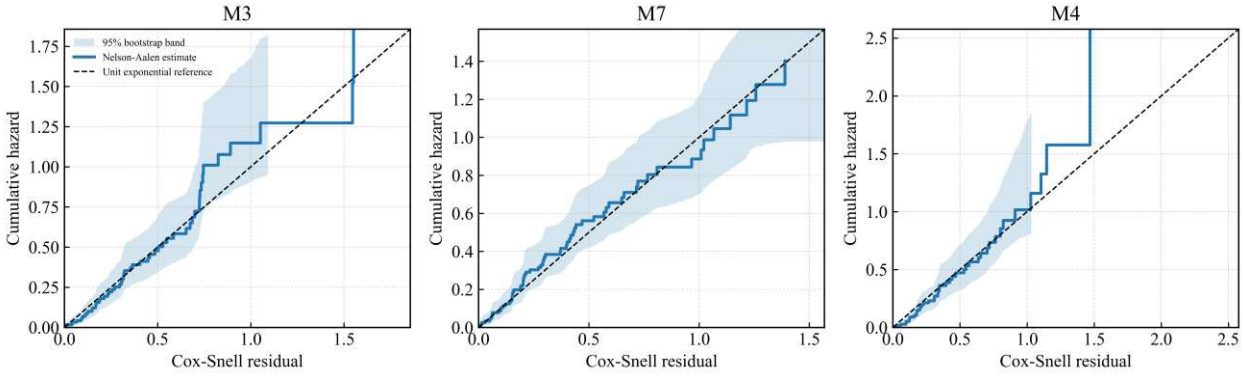


Figure 9. Cox–Snell residual diagnostic plots for the main representative modes.

Table 9. Summary of Cox-Snell residual samples.

Mode	Number of samples	Failures	Right-censored samples	Mean residual	Median residual
M_3	120	54	66	0.433	0.305
M_7	120	64	56	0.524	0.386
M_4	120	42	78	0.350	0.215

The diagnostic curves approximately followed the unit-slope reference line over the main residual range, indicating that the fitted lifetime and aging-corrected survival models were acceptable for the engineering demonstration. Moderate deviations appeared in the tail region, which is reasonable because the number of observed failures was limited and part of the data was right-censored.

Sensitivity of reliability to aging-correction coefficients

Variance-based global sensitivity analysis was performed for the key aging-correction coefficients. The complete-model reliability was used as the model output. The Sobol total-order sensitivity indices are shown in Figure 10.

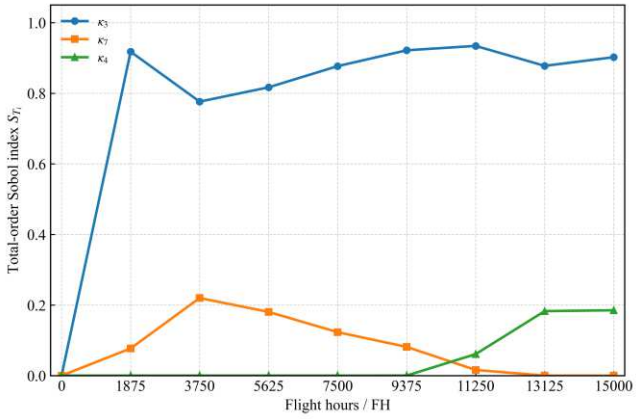


Figure 10. Sobol total-order sensitivity indices of aging-correction coefficients.

The results show that the fretting-related aging coefficient κ_3 was the dominant contributor to reliability uncertainty. The disk-slot cracking coefficient κ_4 and the creep-related coefficient κ_7 had smaller but still observable effects. This result is consistent with the representative-mode evolution identified by the dynamic PNET procedure: M_3 remained the main representative mode over most of the service interval, while M_7 and M_4 acted as secondary representative modes at different service stages.

From an engineering perspective, this finding suggests that uncertainty reduction should prioritize the characterization of contact-interface degradation. Inspection information related to fretting traces, local wear,

frictional oxidation, contact pressure and attachment-region stress concentration would be particularly useful for improving reliability prediction.

Gaussian-copula Monte Carlo benchmark

An exploratory Gaussian-copula Monte Carlo benchmark was performed to examine the possible effect of joint dependence among failure modes. The benchmark results are summarized in Table 10 and Figure 11.

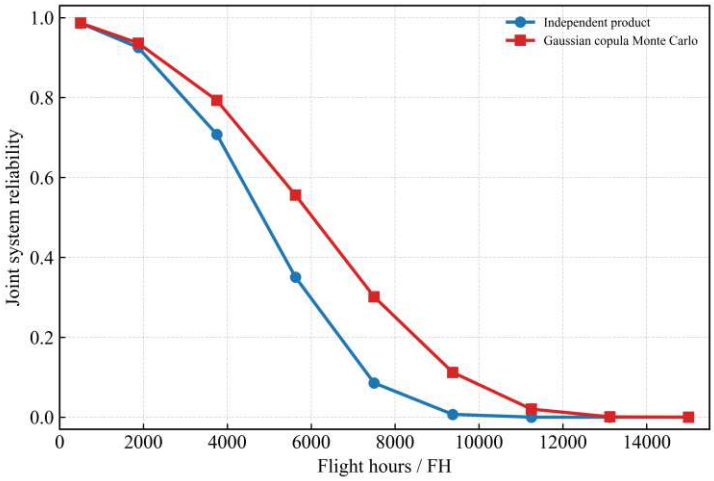


Figure 11. Comparison between the independent product model and the Gaussian-copula Monte Carlo benchmark.

Table 10. Gaussian-copula Monte Carlo joint reliability benchmark.

FH	Independent product Model A	Gaussian copula MC benchmark	MC standard error	95% MC interval
500	9.861×10^{-1}	9.865×10^{-1}	2.108×10^{-4}	$[9.861\times10^{-1},9.869\times10^{-1}]$
1875	9.253×10^{-1}	9.361×10^{-1}	4.464×10^{-4}	$[9.353\times10^{-1},9.370\times10^{-1}]$
3750	7.077×10^{-1}	7.929×10^{-1}	7.399×10^{-4}	$[7.914\times10^{-1},7.943\times10^{-1}]$
5625	3.504×10^{-1}	5.560×10^{-1}	9.071×10^{-4}	$[5.542\times10^{-1},5.578\times10^{-1}]$
7500	8.563×10^{-2}	3.015×10^{-1}	8.378×10^{-4}	$[2.998\times10^{-1},3.031\times10^{-1}]$
9375	6.996×10^{-3}	1.121×10^{-1}	5.761×10^{-4}	$[1.110\times10^{-1},1.133\times10^{-1}]$
11250	9.268×10^{-5}	2.015×10^{-2}	2.566×10^{-4}	$[1.965\times10^{-2},2.066\times10^{-2}]$
13125	5.303×10^{-8}	7.700×10^{-4}	5.064×10^{-5}	$[6.707\times10^{-4},8.693\times10^{-4}]$
15000	1.375×10^{-13}	0 observed survivors	Not estimable by plug-in formula	<3/N

The Gaussian-copula benchmark was higher than the independent product model over most of the service interval. This confirms that the independent product approximation may underestimate system reliability when failure modes are positively dependent, because common-cause risks can be counted repeatedly. However, the copula parameters were not estimated from fully observed joint lifetime samples. Therefore, this benchmark is used only as a robustness comparison and not as the primary reliability estimate.

Threshold and centrality-weight sensitivity analysis

Threshold and centrality-weight sensitivity analyses were performed using the aggregated dependence-similarity matrix at 5000 FH. The results are reported in Table 11.

Table 11. Sensitivity of representative-mode selection to graph threshold and centrality weight.

Graph threshold r	Centrality weight α	Number of clusters	Clusters	Representative modes
0.58	0.3	1	$\{M_1, M_2, M_3, M_4, M_5, M_6, M_7\}$	$\{M_3\}$
0.58	0.5	1	$\{M_1, M_2, M_3, M_4, M_5, M_6, M_7\}$	$\{M_3\}$
0.58	0.7	1	$\{M_1, M_2, M_3, M_4, M_5, M_6, M_7\}$	$\{M_3\}$
0.60	0.3	2	$\{M_1, M_2, M_3, M_5, M_6\};\{M_4, M_7\}$	$\{M_3, M_7\}$
0.60	0.5	2	$\{M_1, M_2, M_3, M_5, M_6\};\{M_4, M_7\}$	$\{M_3, M_7\}$
0.60	0.7	2	$\{M_1, M_2, M_3, M_5, M_6\};\{M_4, M_7\}$	$\{M_3, M_7\}$
0.62	0.3	2	$\{M_1, M_2, M_3, M_5, M_6\};\{M_4, M_7\}$	$\{M_3, M_7\}$
0.62	0.5	2	$\{M_1, M_2, M_3, M_5, M_6\};\{M_4, M_7\}$	$\{M_3, M_7\}$
0.62	0.7	2	$\{M_1, M_2, M_3, M_5, M_6\};\{M_4, M_7\}$	$\{M_3, M_7\}$
0.65	0.3	3	$\{M_1, M_2, M_3, M_5, M_6\};\{M_4\};\{M_7\}$	$\{M_3, M_4, M_7\}$
0.65	0.5	3	$\{M_1, M_2, M_3, M_5, M_6\};\{M_4\};\{M_7\}$	$\{M_3, M_4, M_7\}$
0.65	0.7	3	$\{M_1, M_2, M_3, M_5, M_6\};\{M_4\};\{M_7\}$	$\{M_3, M_4, M_7\}$
0.70	0.3	3	$\{M_1, M_2, M_3, M_5, M_6\};\{M_4\};\{M_7\}$	$\{M_3, M_4, M_7\}$
0.70	0.5	3	$\{M_1, M_2, M_3, M_5, M_6\};\{M_4\};\{M_7\}$	$\{M_3, M_4, M_7\}$
0.70	0.7	3	$\{M_1, M_2, M_3, M_5, M_6\};\{M_4\};\{M_7\}$	$\{M_3, M_4, M_7\}$

The representative-mode structure remained stable across the tested centrality weights. For $r = 0.60$ and $r = 0.62$, the selected representative modes were consistently $\{M_3, M_7\}$. For $r = 0.65$ and $r = 0.70$, M_4 became an independent representative mode, and the selected representative set changed to $\{M_3, M_4, M_7\}$. When $r = 0.58$, all modes were merged into one cluster, and M_3 was selected as the sole representative mode.

Overall, the robustness checks support the stability of the proposed representative-mode screening procedure. The main contact-coupled degradation group was consistently represented by M_3, while the separation of M_4 and M_7 depended mainly on the graph threshold. This behavior is consistent with the physical interpretation that fretting-related attachment degradation is the central common-risk path, whereas disk-slot cracking and creep-related degradation form secondary paths whose separation becomes clearer under stricter dependence-similarity thresholds.

Discussion

The proposed framework combines two types of information that are often treated separately in reliability modelling: dependence among failure modes and mechanism-informed aging acceleration. The case study shows that these two mechanisms influence reliability estimates in different directions. Dependence-aware PNET increases the reliability estimate relative to the full-mode independent product because it reduces repeated counting of positively dependent or physically similar failure paths. In contrast, equivalent damage-time correction decreases reliability because it evaluates each mechanism on an accelerated damage scale rather than on calendar flight hours alone.

This distinction is important for engineering interpretation. A low reliability estimate may arise because the component is genuinely aging faster under severe service conditions, or because the model has multiplied several correlated degradation paths as if they were independent. By separating PNET screening from aging correction, the proposed four-model comparison framework helps distinguish these two effects.

The stable selection of tenon fretting wear as the representative mode of the main cluster indicates that contact-interface degradation plays a central role in the blade-attachment degradation group. This does not mean that other modes in the cluster are unimportant. Rather, it means that this mode has the highest combined score in terms of instantaneous risk and dependence similarity within the screened group. From a maintenance perspective, monitoring of contact conditions, fretting traces, local wear, oxidation and attachment-region stress indicators should be prioritized.

The late-service transition from creep rupture to disk slot cracking in the secondary cluster suggests that the relative importance of degradation mechanisms can change as accumulated damage, contact conditions and local stress redistribution evolve. Therefore, a fixed representative-mode set may be insufficient for long-life components subjected to variable operating profiles.

The composite dependence-similarity score should be interpreted carefully. It is not a direct probability of joint failure and should not be used as a Pearson correlation or copula parameter. Its purpose is engineering screening: to identify modes that are sufficiently related through common loads, similar failure rates or overlapping lifetime distributions to justify representative-mode reduction. This distinction is particularly important because the score intentionally combines statistical dependence and marginal similarity information.

The aging correction coefficients should also be interpreted within their modelling assumptions. The linear relation $\tau_i(t) = \kappa_i t$ provides a practical average damage-time transformation, but it does not replace detailed physics-of-failure models. For mechanisms such as fretting fatigue, creep and thermomechanical fatigue, the actual damage process may depend nonlinearly on stress amplitude, contact pressure, temperature, dwell time, slip amplitude and environmental exposure. The present model therefore provides an intermediate engineering approximation between purely statistical lifetime modelling and fully resolved physics-based damage simulation.

Several limitations remain. First, the case study uses sanitized and aggregated fleet data, and raw engine-level histories are not publicly available because of confidentiality restrictions. Second, the decomposed common-load dependence, failure-rate-proximity and lifetime-overlap matrices cannot be fully released, limiting public reproduction of complete weight-ablation experiments. Third, the equivalent damage-time correction uses average aging coefficients rather than detailed time-varying load spectra. Fourth, the case study is limited to one blade-disk assembly configuration. Additional validation using independent fleets, different engine types and fully resolved operational histories is required before broader engineering deployment.

Despite these limitations, the proposed framework provides a practical way to organize dependent multi-mode degradation information under industrial data constraints. It is especially useful when full joint lifetime distributions are difficult to estimate, but marginal lifetime models, inspection records and aggregated load-environment indicators are available.

Conclusions

This study proposed a dynamic reliability assessment framework for aero-engine hot-section components by integrating dependence-aware PNET and mechanism-informed equivalent damage-time correction.

The main conclusions are as follows:

A composite dependence-similarity score was developed by combining common-load-induced dependence, failure-rate proximity and lifetime-distribution overlap. This score provides an interpretable basis for graph-based screening of correlated or physically similar failure modes.

A dynamic PNET procedure was established to update failure-mode clusters and representative modes at discrete service-time nodes. In the blade-disk assembly case study, the method substantially reduced the dimension of the multi-mode reliability problem while retaining the dominant degradation paths.

A general four-model comparison framework was defined in the methodology. The framework distinguishes the effects of full-mode independent modelling, representative-mode screening, aging correction and their combination.

The case study showed that the representative mode of the main blade-attachment cluster remained associated with fretting-related contact-interface degradation, while the representative mode of the secondary cluster shifted from creep-related degradation to disk-slot cracking in late service.

Mechanism-informed equivalent damage-time correction accounted for accelerated degradation under actual operating profiles. The fretting-related aging coefficient was the dominant contributor to uncertainty in complete-model reliability.

The comparison of four reliability models demonstrated the complementary roles of PNET screening and aging correction. Dependence screening mitigated repeated counting of positively dependent failure paths, whereas aging correction reduced reliability by accounting for accelerated damage accumulation.

The proposed framework offers an interpretable and extensible approach for reliability assessment of dependent degradation processes in aero-engine components. Future work should incorporate detailed load spectra, online health-monitoring data, hierarchical estimation of aging coefficients and validation using multiple independent fleets.

References

1. Boyce, M. P. Gas Turbine Engineering Handbook 4th edn (Butterworth-Heinemann, 2012).
2. Reed, R. C. The Superalloys: Fundamentals and Applications (Cambridge University Press, 2006).
3. Pollock, T. M. & Tin, S. Nickel-based superalloys for advanced turbine engines: chemistry, microstructure and properties. J. Propuls. Power 22, 361–374 (2006).
4. Pineau, A. & Antolovich, S. D. High temperature fatigue of nickel-base superalloys—a review with special emphasis on deformation modes and oxidation. Eng. Fail. Anal. 16, 2668–2697 (2009).
5. Evans, A. G., Mumm, D. R., Hutchinson, J. W., Meier, G. H. & Pettit, F. S. Mechanisms controlling the durability of thermal barrier coatings. Prog. Mater. Sci. 46, 505–553 (2001).
6. Suresh, S. Fatigue of Materials 2nd edn (Cambridge University Press, 1998).
7. Nicholas, T. High Cycle Fatigue: A Mechanics of Materials Perspective (Elsevier, 2006).
8. Tong, J., Dalby, S., Byrne, J., Henderson, M. B. & Hardy, M. C. Creep, fatigue and oxidation in crack growth in advanced nickel base superalloys. Int. J. Fatigue 23, 897–902 (2001).
9. Hills, D. A. & Nowell, D. Mechanics of Fretting Fatigue (Kluwer Academic Publishers, 1994).
10. Golden, P. J. Development of a dovetail fretting fatigue fixture for turbine engine materials. Int. J. Fatigue 31, 620–628 (2009).
11. Iyer, K. Peak contact pressure, cyclic stress amplitudes, contact semi-width and slip amplitude: relative effects on fretting fatigue life. Int. J. Fatigue 23, 193–206 (2001).
12. Peters, J. O. et al. On the application of the Kitagawa–Takahashi diagram to foreign-object damage and high-cycle fatigue. Eng. Fract. Mech. 69, 1425–1446 (2002).
13. Ditlevsen, O. Narrow reliability bounds for structural systems. J. Struct. Mech. 7, 453–472 (1979).
14. Ditlevsen, O. & Madsen, H. O. Structural Reliability Methods (John Wiley & Sons, 1996).
15. Melchers, R. E. & Beck, A. T. Structural Reliability Analysis and Prediction 3rd edn (John Wiley & Sons, 2018).
16. Ma, H.-F. & Ang, A. H.-S. Reliability Analysis of Redundant Ductile Structural Systems. Structural Research Series No. 494 (University of Illinois at Urbana–Champaign, 1981).
17. Ang, A. H.-S. & Tang, W. H. Probability Concepts in Engineering: Emphasis on Applications to Civil and Environmental Engineering 2nd edn (John Wiley & Sons, 2007).
18. Zhang, Z., Si, X., Hu, C. & Lei, Y. Degradation data analysis and remaining useful life estimation: a review on Wiener-process-based methods. Eur. J. Oper. Res. 271, 775–796 (2018).
19. Yi, H., Zhang, W., Wang, G., Zhang, X. & Zhai, Q. Statistical multivariate degradation modeling—a systematic review. Reliab. Eng. Syst. Saf. 264, 111286 (2025).
20. Yang, C., Gu, X. & Zhao, F. Reliability analysis of degrading systems based on time-varying copula. Microelectron. Reliab. 136, 114628 (2022).
21. Nelsen, R. B. An Introduction to Copulas 2nd edn (Springer, 2006).
22. Miner, M. A. Cumulative damage in fatigue. J. Appl. Mech. 12, A159–A164 (1945).

23. Lemaitre, J. & Chaboche, J.-L. Mechanics of Solid Materials (Cambridge University Press, 1990).
24. Dowling, N. E. Mechanical Behavior of Materials: Engineering Methods for Deformation, Fracture, and Fatigue 4th edn (Pearson, 2013).
25. Fatemi, A. & Yang, L. Cumulative fatigue damage and life prediction theories: a survey of the state of the art for homogeneous materials. Int. J. Fatigue 20, 9–34 (1998).
26. Nelson, W. Accelerated Testing: Statistical Models, Test Plans, and Data Analysis (John Wiley & Sons, 1990).
27. Meeker, W. Q. & Escobar, L. A. Statistical Methods for Reliability Data (John Wiley & Sons, 1998).
28. Larson, F. R. & Miller, J. A time-temperature relationship for rupture and creep stresses. Trans. ASME 74, 765–771 (1952).
29. Hanumanthan, H., Stitt, A., Laskaridis, P. & Singh, R. Severity estimation and effect of operational parameters for civil aircraft jet engines. Proc. Inst. Mech. Eng. Part G J. Aerosp. Eng. 226, 1544–1561 (2012).
30. Naeem, M. Impacts of low-pressure (LP) compressor's deterioration upon an aero-engine's high-pressure (HP) turbine blade's life consumption. Aeronaut. J. 110, 227–238 (2006).
31. Jardine, A. K. S., Lin, D. & Banjevic, D. A review on machinery diagnostics and prognostics implementing condition-based maintenance. Mech. Syst. Signal Process. 20, 1483–1510 (2006).
32. Tahan, M., Tsoutsanis, E., Muhammad, M. & Abdul Karim, Z. A. Performance-based health monitoring, diagnostics and prognostics for condition-based maintenance of gas turbines: a review. Appl. Energy 198, 122–144 (2017).
33. Lei, Y. et al. Machinery health prognostics: a systematic review from data acquisition to RUL prediction. Mech. Syst. Signal Process. 104, 799–834 (2018).
34. Kaplan, E. L. & Meier, P. Nonparametric estimation from incomplete observations. J. Am. Stat. Assoc. 53, 457–481 (1958).
35. Cox, D. R. & Snell, E. J. A general definition of residuals. J. R. Stat. Soc. Ser. B 30, 248–265 (1968).
36. Akaike, H. A new look at the statistical model identification. IEEE Trans. Autom. Control 19, 716–723 (1974).
37. Inman, H. F. & Bradley, E. L. The overlapping coefficient as a measure of agreement between probability distributions and point estimation of the overlap of two normal densities. Commun. Stat. Theory Methods 18, 3851–3874 (1989).
38. Nelson, W. Theory and applications of hazard plotting for censored failure data. Technometrics 14, 945–966 (1972).
39. Aalen, O. Nonparametric inference for a family of counting processes. Ann. Stat. 6, 701–726 (1978).
40. Sobol', I. M. Global sensitivity indices for nonlinear mathematical models and their Monte Carlo estimates. Math. Comput. Simul. 55, 271–280 (2001).
41. Saltelli, A. et al. Variance based sensitivity analysis of model output. Design and estimator for the total sensitivity index. Comput. Phys. Commun. 181, 259–270 (2010).

Acknowledgements

This work was supported by the Key International Cooperation Project of the National Natural Science Foundation of China (Grant No. W2511076).